

# Electrically Tunable Macroscopic Quantum Tunneling in a Graphene-Based Josephson Junction

Gil-Ho Lee,<sup>1</sup> Dongchan Jeong,<sup>1</sup> Jae-Hyun Choi,<sup>1,\*</sup> Yong-Joo Doh,<sup>2,†</sup> and Hu-Jong Lee<sup>1,‡</sup>

<sup>1</sup>Department of Physics, Pohang University of Science and Technology, Pohang 790-784, Republic of Korea

<sup>2</sup>Department of Display and Semiconductor Physics, Korea University Sejong Campus, Chungnam 339-700, Republic of Korea

(Received 19 May 2011; published 30 September 2011)

Stochastic switching-current distribution in a graphene-based Josephson junction exhibits a crossover from the classical to quantum regime, revealing the macroscopic quantum tunneling of a Josephson phase particle at low temperatures. Microwave spectroscopy measurements indicate a multiphoton absorption process occurring via discrete energy levels in washboard potential well. The crossover temperature for macroscopic quantum tunneling and the quantized level spacing are controlled with the gate voltage, implying its potential application to gate-tunable superconducting quantum bits.

DOI: 10.1103/PhysRevLett.107.146605

PACS numbers: 72.80.Vp, 73.40.-c, 74.45.+c, 85.25.Cp

A Josephson junction [1], consisting of two superconducting electrodes connected to each other via a nonsuperconducting spacer, provides the basic building block of superconducting quantum bits (qubits) [2] for constructing scalable solid-state quantum computers [3]. Recent advances in nanofabrication techniques have enabled the fabrication of nanostructured proximity-coupled Josephson junctions based on conducting spacers such as nanowires [4,5], carbon nanotubes [6,7], nanocrystals [8], and graphene [9]. In contrast to typical tunneling or weak-link [10] Josephson junctions, the Josephson coupling energy in nanostructured Josephson junctions can be tuned electrically for applications in quantum supercurrent transistors [4–6].

In this Letter, we report the stochastic switching-current distribution in a superconductor-graphene-superconductor (SGS) junction, demonstrating macroscopic quantum tunneling (MQT) [11,12] behavior at low temperatures and energy-level quantization [12] in a potential well for a Josephson phase particle. The crossover temperature for MQT and the energy-level separation are controlled by applying a gate voltage to the SGS junction. Observation of this gate tunability of the quantum phenomena, first in proximity-coupled Josephson junctions, is mainly indebted to the gate-tunable Josephson coupling energy in the SGS junction. Our findings are relevant to enhanced degrees of freedom for manipulating the macroscopic quantum state in a Josephson junction and to the development of a new type of quantum devices such as a gate-tunable superconducting phase qubit.

SGS hybrid devices were assembled from single-layer graphene in contact with superconducting  $\text{Pb}_{0.93}\text{In}_{0.07}$  (PbIn) electrodes. We alloyed Pb with In to minimize the granularity of electrodes while keeping  $T_c$  almost intact [13,14]. Figure 1(a) shows a representative optical microscopy image of the PbIn-graphene-PbIn Josephson junction. PbIn superconducting electrodes significantly enhances the critical current ( $I_c$ ) compared with commonly used Al (as high as  $I_c \sim 6.0 \mu\text{A}$  in highly doped regions) for

both the electron and hole side at the base temperature ( $T = 50 \text{ mK}$ ). This leads to a much stronger Josephson coupling energy  $E_J = \hbar I_c / 2e$ , where  $\hbar$  is Planck's constant ( $h$ ) divided by  $2\pi$ . The normal-state resistance ( $R_N$ ) of the SGS Josephson junction exhibits a charge-neutral Dirac point occurring at the back-gate voltage ( $V_{bg}$ ) of  $V_{DP} = -2.5 \text{ V}$  [inset of Fig. 1(b)]. The corresponding

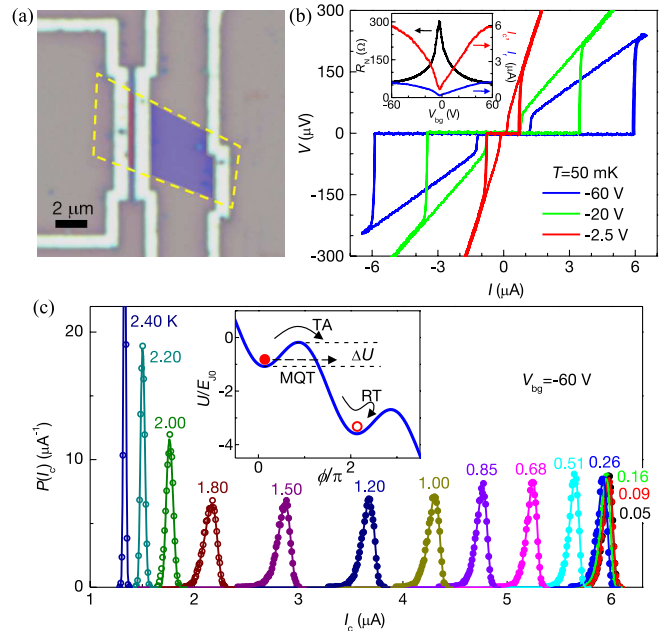


FIG. 1 (color online). (a) Optical image of the device. A graphene flake was placed in the region bound by the yellow dotted line, and the junction area is denoted in red. (b) Typical  $I$ - $V$  curves for various  $V_{bg}$  at  $T = 50 \text{ mK}$ . Inset:  $V_{bg}$  dependence of  $R_N$  (black),  $I_c$  (red), and  $I_r$  (blue).  $R_N$  was measured in a perpendicular magnetic field of  $H = 50 \text{ mT}$ . (c)  $I_c$  distribution obtained at  $V_{bg} = -60 \text{ V}$ . Solid lines are best fits to the thermal activation (TA, solid symbols) and phase diffusion (PD, void symbols) models. Inset: Schematic of washboard potential and dynamics of a phase particle escaping from the local minimum.

mean free path and diffusion constant of the graphene layer are estimated to be  $l_m^* \sim 22$  nm and  $D \sim 110$  cm<sup>2</sup>/s, respectively [14]. Because  $l_m^*$  and the Thouless energy ( $E_{\text{Th}} = \hbar D/L^2 \sim 80$   $\mu$ eV) are much smaller than the junction spacing of  $L = 300$  nm and the superconducting energy gap of  $\Delta_{\text{PbIn}} = 1.1$  meV, respectively, our SGS junctions are subject to a long diffusive junction limit [15].

The current-voltage ( $I$ - $V$ ) curves for different  $V_{\text{bg}}$  in the superconducting state at the base temperature [Fig. 1(b)] exhibit hysteresis for the switching currents of  $I_c$  (from the supercurrent branch to the resistive branch) and  $I_r$  (vice versa). Hysteretic behavior is common in SGS junctions [9]. It also has been observed in other nanostructured Josephson junctions [4–7], where it was attributed to self-heating [16] or an effective capacitance ( $C_{\text{eff}} = \hbar/R_N E_{\text{Th}}$ ) due to diffusive motion of quasiparticles in graphene [17]. Our numerical calculations based on the resistively and capacitively shunted junction model [18] fit the data well with a finite junction capacitance  $C$  [14]. Thus, the switching-current distribution  $P(I_c)$  in our SGS junction [14] is explicable in terms of underdamped-junction motion of a fictitious phase particle in a tilted-washboard potential [18] [inset of Fig. 1(c)]. Here, the mass of the phase particle is proportional to  $C$ , and it is assumed to move in a metastable potential well of  $U(\phi) = -E_{J0}[\cos(\phi) + (I/I_{c0})]$ , where  $\phi$  is the phase difference across the junction and  $I_{c0}$  and  $E_{J0}(= \hbar I_{c0}/2e)$  are the fluctuation-free switching current and Josephson coupling energy, respectively. The escape rate of a phase particle from the potential well corresponds to the switching rate from the supercurrent state to the resistive state, which is governed by the Josephson coupling energy and thermal and quantum fluctuations.

$P(I_c)$  in our SGS junction is shown in Fig. 1(c) for  $T = 0.05$ – $2.40$  K at  $V_{\text{bg}} = -60$  V, where three distinct temperature regions are identified. For  $T > 1.80$  K, a symmetric, narrow  $P(I_c)$  is obtained, which broadens with decreasing  $T$ . For  $0.51$  K  $< T < 1.80$  K, the distribution is asymmetric, and the width narrows with decreasing  $T$ ; this  $T$  dependence is opposite to that for  $T > 1.80$  K. For  $T < 0.26$  K, the shape and width of  $P(I_c)$  are nearly independent of  $T$ . Theoretical fits lead to the conclusion that each of the three temperature regions corresponds to the phase diffusion (PD) [19,20], thermal activation (TA) [21], and MQT [12] of a phase particle, respectively. In this Letter, we focus on the TA and MQT regimes, and the PD regime is discussed in the Supplemental Material [14].

In the TA regime, switching from the superconducting to the resistive state occurs via thermally activated escape of the phase particle from a local minimum of a tilted-washboard potential. For quantitative analysis, the switching probability of the relationship  $P(I_c) = [\Gamma(I_c)/(dI/dt)]\{1 - \int_0^{I_c} P(I')dI'\}$  is used [21], where  $dI/dt$  is the current-sweeping rate and  $\Gamma$  is the escape rate. The rate of thermal escape is given by

$\Gamma_{\text{TA}} = a_i(\omega_p/2\pi)\exp[-\Delta U/k_B T]$ , where  $a_i = (1 + 1/4Q^2)^{1/2} - 1/2Q$  is a damping-dependent factor,  $\omega_p = \omega_{p0}(1 - \gamma^2)^{1/4}$ , and  $\Delta U = 2E_{J0}[(1 - \gamma^2)^{1/2} - \gamma\cos^{-1}\gamma]$ , with the quality factor  $Q = 4I_c/\pi I_r$ , a Josephson plasma frequency  $\omega_{p0} = (2eI_{c0}/\hbar C)^{1/2}$ , and  $\gamma = I/I_{c0}$ . It is noted that the normalized standard deviation (SD) of  $P(I_c)$  decreases with decreasing  $T$  [Fig. 2(a)].

In the MQT regime, however, the escape of the phase particle is governed by the tunneling process with a rate [12] of  $\Gamma_{\text{MQT}} = 12\omega_p(3\Delta U/\hbar\omega_p)^{1/2}\exp[-7.2(1 + 0.87/Q)\Delta U/\hbar\omega_p]$ . As  $\Gamma_{\text{MQT}}$  is independent of  $T$ , the normalized SD of  $P(I_c)$  in the MQT regime does not vary with  $T$  [Fig. 2(a)]. Thus, the  $P(I_c)$  and  $\Gamma(I_c)$  curves for different  $T$  are essentially identical in the MQT regime [see Figs. 1(c) and 2(b)]. The best fit of the escape-rate data to the expression of  $\Gamma_{\text{MQT}}$  results in  $I_{c0} = 7.00$   $\mu$ A and a junction capacitance of  $C = 11.5$  fF. More details of phase-particle escape fitting are given in the Supplemental Material [14].

Fitting the  $P(I_c)$  data to the TA model over the entire temperature range of our study reveals the escape temperature ( $T_{\text{esc}}$ ), i.e., the temperature perceived by the escaping phase particle. A direct comparison between  $T_{\text{esc}}$  and  $T$  [inset of Fig. 2(a)] shows saturation of  $T_{\text{esc}}$  in the MQT regime and an almost linear increase of  $T_{\text{esc}}$  with  $T$  in the TA regime. The saturation of  $T_{\text{esc}}$  corresponds to

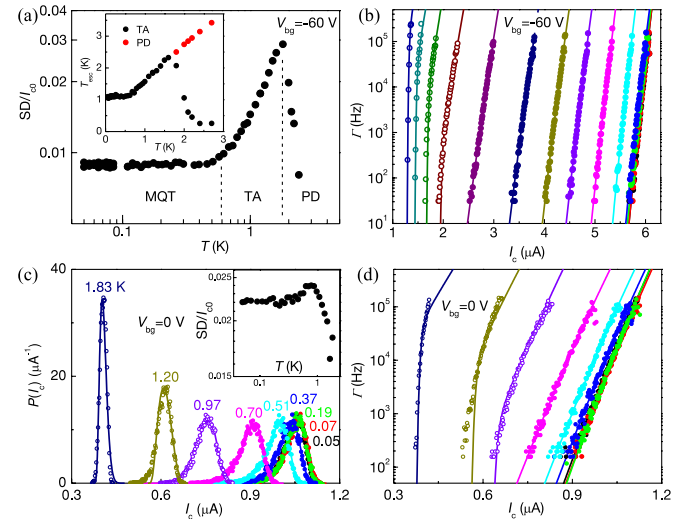


FIG. 2 (color online). (a)  $T$  dependence of the normalized SD of the  $I_c$  distribution,  $P(I_c)$ , obtained for  $V_{\text{bg}} = -60$  V. Inset:  $T_{\text{esc}}$  versus  $T$  plot obtained from a fit to the TA (black) and PD (red) models. The error bars are smaller than the symbol size. (b) Escape rate  $\Gamma$  (symbols) as a function of bias current at  $V_{\text{bg}} = -60$  V. Solid lines represent fits to the TA (filled symbols) and PD (void symbols) models. Each data set corresponds to the one in Fig. 1(c) with the same color code. (c)  $I_c$  distribution obtained for varying  $T$  at  $V_{\text{bg}} = 0$  V. The rightmost three curves are not distinguishable. Inset:  $T$  dependence of the normalized standard deviation. (d) Escape rate (symbols) overlaid with best-fit curves to the TA (filled symbols) and PD (void symbols) models.

the temperature region where the TA model fails. The crossover temperature between the two regimes is consistent with that obtained from the normalized SD of  $P(I_c)$ . With increasing  $T$ , a sudden decrease in  $T_{\text{esc}}$  occurs at  $T = 1.8$  K, again implying a failure of the TA model at high  $T$ . A new fit based on the PD model remedies the discrepancy.  $T_{\text{esc}}$  is higher than  $T$  by  $\sim 0.5$  K in the TA regime, implying that  $\Delta U$  is slightly overestimated in the fit. A nonsinusoidal current-phase relationship [22] exhibited in the SGS junction most likely causes the deviation of  $T_{\text{esc}}$  from  $T$ .

Figure 2(c) shows the  $T$  dependence of  $P(I_c)$  curves at  $V_{\text{bg}} = 0$  V near  $V_{\text{DP}}$ , displaying a gradual change in the distribution, the overall shape of which is similar to those obtained from the highly doped region at  $V_{\text{bg}} = -60$  V. The normalized SD of  $P(I_c)$  in the inset exhibits broadening (PD regime), narrowing (TA regime), and saturation (MQT regime) behaviors with decreasing  $T$ . Our data fit well with each model in the corresponding  $T$  range [see Figs. 2(c) and 2(d)]. Despite the overall similarity between the two data sets of  $P(I_c)$  with different  $V_{\text{bg}}$ , crossover temperatures between the two escape processes (MQT-TA or TA-PD) are suppressed as  $V_{\text{bg}}$  approaches  $V_{\text{DP}}$  (see below). The theoretical fit results in values of  $I_{c0}$  ( $= 1.91$   $\mu\text{A}$ ) and  $C$  ( $= 2.4$  fF) that are lower than those obtained at  $V_{\text{bg}} = -60$  V.

Figure 3(a) shows the progressive change in the normalized SD versus  $T$  curve with varying  $V_{\text{bg}}$ . The crossover

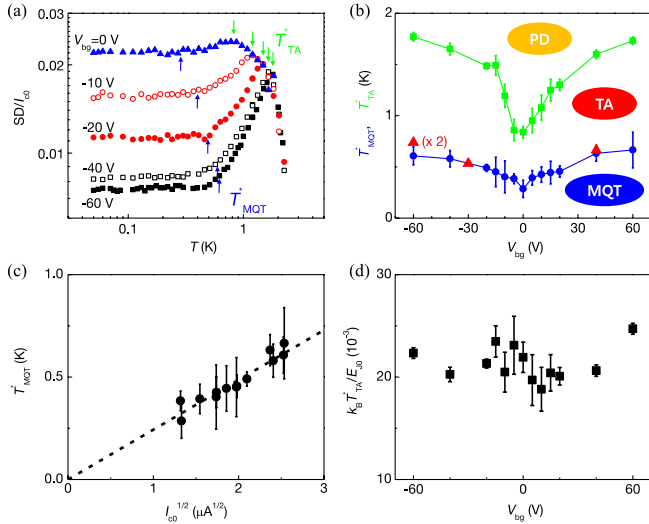


FIG. 3 (color online). (a) Normalized SD versus  $T$  plot with  $V_{\text{bg}} = -60, -40, -20, -10,$  and  $0$  V from bottom to top. Arrows indicate  $T_{\text{MQT}}^*$  and  $T_{\text{TA}}^*$  for each value of  $V_{\text{bg}}$ . (b)  $V_{\text{bg}}$  dependence of the crossover temperatures of  $T_{\text{MQT}}^*$  (blue circle) and  $T_{\text{TA}}^*$  (green square).  $T_{\text{MQT}}^*$  estimated from microwave spectroscopy measurements are also shown, multiplied by a factor of 2 (red triangle). (c) Proportionality relationship between  $T_{\text{MQT}}^*$  and  $I_{c0}^{1/2}$ . The dotted line is a guide for the eyes. (d)  $T_{\text{TA}}^*$  normalized by  $E_{J0}$  as a function of  $V_{\text{bg}}$ .

temperature  $T_{\text{MQT}}^*$  ( $T_{\text{TA}}^*$ ) between the MQT (TA) and TA (PD) regimes can be defined as the crossing point of two lines extrapolated from each regime. As the applied  $V_{\text{bg}}$  approaches  $V_{\text{DP}}$ ,  $T_{\text{MQT}}^*$  and  $T_{\text{TA}}^*$  decrease and the crossover regions broaden gradually.

The crossover temperatures that separate the three distinct regions of PD, TA, and MQT vary with  $V_{\text{bg}}$  [Fig. 3(b)]. Both  $T_{\text{MQT}}^*$  and  $T_{\text{TA}}^*$  decrease sharply near  $V_{\text{DP}}$ , indicating that the escape of a phase particle from the washboard potential can be tuned by applying  $V_{\text{bg}}$ . This constitutes the central observation of this study, the physical origin of which stems from the gate tunability of  $E_{J0}$  by  $V_{\text{bg}}$  in an SGS junction. Theoretically,  $T_{\text{TA}}^*$  is linearly proportional to  $E_{J0}$  via the relationship [23]  $T_{\text{TA}}^* \sim E_{J0} [1 - (4/\pi Q)]^{3/2} / 30k_B$ . Because  $Q$  varies smoothly as a function of  $V_{\text{bg}}$  between 5 (near  $V_{\text{DP}}$ ) and 6 (for  $V_{\text{bg}} \approx \pm 60$  V), the ratio of  $k_B T_{\text{TA}}^* / E_{J0}$  is nearly independent of  $V_{\text{bg}}$  [Fig. 3(d)]. Thus,  $T_{\text{TA}}^*$  is determined almost solely by the  $V_{\text{bg}}$  dependence of  $E_{J0}$ .  $T_{\text{MQT}}^*$  is related to  $\omega_p$  as [24]  $T_{\text{MQT}}^* = a_1 \hbar \omega_p / 2\pi k_B$ . Because  $\omega_{p0}$  is proportional to  $I_{c0}^{1/2}$ , the resulting relationship  $T_{\text{MQT}}^* \propto I_{c0}^{1/2}$  [Fig. 3(c)] gives a qualitative explanation for the  $V_{\text{bg}}$  dependence of  $T_{\text{MQT}}^*$ . The junction capacitance  $C^* = 35.2$  fF estimated from  $T_{\text{MQT}}^*$  at  $V_{\text{bg}} = -60$  V is comparable to the result obtained from the  $\Gamma_{\text{MQT}}$  fit.

In the MQT regime, the energy levels in the potential well are presumed to be quantized with a level spacing of  $E_{10}$  between the ground and the first excited states [12]. For irradiation with microwaves of frequency  $f_{\text{mw}}$  corresponding to the photon energy equal to the quantized level spacing ( $E_{10} = \hbar f_{\text{mw}}$ ), tunneling of a phase particle is possible via the first excited state. In our SGS junction, a slight increase of the microwave power causes a shift of  $P(I_c)$  to a lower current, intermediated by a double-peaked distribution [Figs. 4(a) and 4(b)], exhibiting a resonant peak at the current  $I_{\text{res}}$ . The occurrence of the resonant peak in  $P(I_c)$  for  $T < T_{\text{MQT}}^*$  is attributed to the MQT process via the first excited state in the potential well, the tunneling rate of which is exponentially enhanced above the direct-tunneling rate from the ground state [12]. The corresponding  $\Gamma(I)$  curve in Fig. 4(c) shows the enhanced tunneling rate at lower current, signifying resonant transitions between the two energy levels.

In a parabolic approximation of the potential well, the energy-level separation depends on the bias current:  $E_{10} = \hbar \omega_{p0} [1 - (I/I_{c0})^2]^{1/4}$ . Because  $\nu_{p0}$  ( $= \omega_{p0} / 2\pi$ ) was substantially higher than  $f_{\text{mw}}$  ( $= 2\text{--}20$  GHz) used in this measurement, a multiphoton absorption process [25,26] ( $E_{10} = n\hbar f_{\text{mw}}$ , where  $n$  is the number of photons) was preferred to a single-photon process, resulting in the resonant-transition condition of  $f_{\text{mw}} = (\nu_{p0}/n) [1 - (I_{\text{res}}/I_{c0})^2]^{1/4}$ . Figure 4(d) displays the observed  $I_{\text{res}}$  with varying  $f_{\text{mw}}$  at  $V_{\text{bg}} = -60$  V, which fits the resonant-condition curves with  $\nu_{p0} = 71.7 \pm 0.5$  GHz

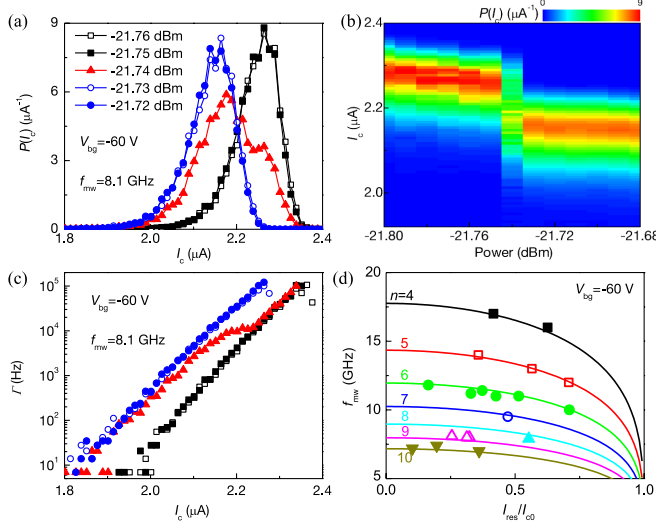


FIG. 4 (color online). (a)  $P(I_c)$  under microwave irradiation of varying power. The microwave frequency was  $f_{mw} = 8.1$  GHz, and  $T = 50$  mK. (b) Color-coded density plot of  $P(I_c)$  with varying microwave power. (c)  $\Gamma(I)$  plot corresponding to the data in (a). (d) Applied microwave frequency  $f_{mw}$  versus normalized resonant bias current  $I_{res}/I_{c0}$  (symbols). Solid lines are best fits to the formula for the multiphoton absorption transition (see the text) with the corresponding number of photons ( $n = 4$ – $10$ ) from top to bottom.

and  $I_{c0} = 8.05 \pm 0.26 \mu\text{A}$  for the number of photons ( $n = 4$ – $10$ ) in our measurement range. As  $\nu_{p0}$  depends on the applied  $V_{bg}$  [14], the quantized energy-level separation in an SGS junction can be tuned not only by the bias current but also by  $V_{bg}$ . From the  $V_{bg}$ -dependent  $\nu_{p0}$ , one can also estimate  $T_{MQT}^*$  for comparison with  $T_{MQT}^*$  from  $P(I_c)$  [see Fig. 3(b)]. Despite the discrepancy between the two different  $T_{MQT}^*$  estimations, the overall  $V_{bg}$  dependence is consistent. We infer that the discrepancy could have been caused by a nonsinusoidal current-phase relationship in the SGS junction [22] and/or incomplete filtering of the environmental noise.

One-dimensional nanostructured proximity Josephson junctions normally support low junction critical currents (for instance,  $\sim 100$  nA for nanowires [4,5] and  $\sim 10$  nA for carbon nanotubes [6,7]). The corresponding weak junction coupling energies,  $E_{J0}/k_B \sim 2$  and  $\sim 0.2$  K, respectively, hamper observation of the MQT and the energy-level quantization in the washboard potential well. By contrast, graphene-based proximity Josephson junctions, in association with the expandable junction width, provide both high gate tunability and strong junction coupling strength (represented by the critical current easily reaching 1–10  $\mu\text{A}$ ), which make graphene-based Josephson junctions a convenient system for observing the gate-tunable quantum behavior. In our device, the junction coupling strength was made even stronger by adopting  $\text{Pb}_{0.93}\text{In}_{0.07}$  superconducting electrodes rather than Al that

is commonly used for realizing graphene-based Josephson junctions. Proximity Josephson junctions based on two-dimensional electron gas are also gate-tunable [20], but the gate tunability of MQT and the energy-level quantization has not been reported in the system.

We thank Dr. M.-H. Bae for providing distribution-fitting codes and helpful discussion. One of us (Y.J.D.) is grateful for useful discussion with M.-S. Choi. This work was supported (for H.J.L.) by National Research Foundation of Korea (NRF) through SRC Centre for Topological Matter (Grant No. 2011-0030046) and Global Frontier Research Center for Advanced Soft Electronics and (for Y.J.D.) through Basic Science Research Program (Grant No. 2011-0005148).

\*Present address: Memory Division, Samsung Electronics, Hwasung 445-701, Republic of Korea.

†yjdo@korea.ac.kr

‡hjlee@postech.ac.kr

- [1] B. D. Josephson, *Phys. Lett.* **1**, 251 (1962).
- [2] J. Clarke and F. K. Wilhelm, *Nature (London)* **453**, 1031 (2008).
- [3] C. H. Bennett and D. P. Divincenzo, *Nature (London)* **404**, 247 (2000).
- [4] Y. J. Doh *et al.*, *Science* **309**, 272 (2005).
- [5] J. Xiang *et al.*, *Nature Nanotech.* **1**, 208 (2006).
- [6] P. Jarillo-Herrero, J. A. van Dam, and L. P. Kouwenhoven, *Nature (London)* **439**, 953 (2006).
- [7] J. P. Cleuziou *et al.*, *Nature Nanotech.* **1**, 53 (2006).
- [8] G. Katsaros *et al.*, *Nature Nanotech.* **5**, 458 (2010).
- [9] H. B. Heersche *et al.*, *Nature (London)* **446**, 56 (2007).
- [10] K. K. Likharev, *Rev. Mod. Phys.* **51**, 101 (1979).
- [11] A. O. Caldeira and A. J. Leggett, *Phys. Rev. Lett.* **46**, 211 (1981).
- [12] J. Clarke *et al.*, *Science* **239**, 992 (1988).
- [13] D. Jeong *et al.*, *Phys. Rev. B* **83**, 094503 (2011).
- [14] See Supplemental Material at <http://link.aps.org/supplemental/10.1103/PhysRevLett.107.146605> for detailed method and data analysis.
- [15] P. Dubos *et al.*, *Phys. Rev. B* **63**, 064502 (2001).
- [16] H. Courtois, M. Meschke, J. T. Peltonen, and J. P. Pekola, *Phys. Rev. Lett.* **101**, 067002 (2008).
- [17] L. Angers *et al.*, *Phys. Rev. B* **77**, 165408 (2008).
- [18] M. Tinkham, *Introduction to Superconductivity* (Dover, New York, 2004).
- [19] J. Männik *et al.*, *Phys. Rev. B* **71**, 220509 (2005).
- [20] V. M. Krasnov *et al.*, *Phys. Rev. Lett.* **95**, 157002 (2005).
- [21] T. A. Fulton and L. N. Dunkleberger, *Phys. Rev. B* **9**, 4760 (1974).
- [22] C. Chialvo *et al.*, arXiv:1005.2630.
- [23] J. M. Kivioja *et al.*, *Phys. Rev. Lett.* **94**, 247002 (2005).
- [24] H. Grabert, P. Olschowski, and U. Weiss, *Phys. Rev. B* **36**, 1931 (1987).
- [25] A. Wallraff, T. Duty, A. Lukashenko, and A. V. Ustinov, *Phys. Rev. Lett.* **90**, 037003 (2003).
- [26] X. Y. Jin *et al.*, *Phys. Rev. Lett.* **96**, 177003 (2006).